

**AlGaN THIN FILMS ON SILICON SUBSTRATES
FOR PHOTODETECTOR AND TRANSISTOR
DEVICES**

By

ASAAD SHAKIR HUSSEIN

**Thesis submitted in fulfillment of the requirements for the degree of
Doctor of Philosophy**

July 2011

ACKNOWLEDGEMENTS

First and foremost, I would like to thank Allah for granting me health and patience to finish this research. I would also like to express my sincere gratitude to my main supervisor, Prof. Zainuriah Hassan, for her scholarly guidance and dedicated time and support throughout the course of this study. I would also like to thank my co-supervisor, Prof. Haslan Abu Hassan, for his valuable guidance and comments on this study.

I also appreciate the help and support offered by Dr. Sabah M. Thahab and Dr. Ng Sha Shiong for their important scientific comments and feedback on my drafts. A special thank goes to the professional editor, Dr. Ghayth al-Shaibani for his valuable academic comments and editing.

Special thanks are due to my colleagues Alaa, Muslim, Osama, Naif and Chin for providing feedback through numerous discussions, and for their help and encouragement.

Much of this work would have been virtually impossible without the technical support offered by our helpful laboratory assistants.

The prayers of my parents, the patience of my wife and children and the support of my brothers and sisters were a powerful source in completing this study. I thank all my friends and colleagues who supported me and helped me at the School of Physics, Universiti Sains Malaysia.

TABLE OF CONTENTS

ACKNOWLEDGEMENTS	ii
TABLE OF CONTENTS	iii
LIST OF TABLES	x
LIST OF FIGURES	xi
LIST OF ABBREVIATIONS	xviii
LIST OF SYMBOLS	xxi
ABSTRAK	xxiv
ABSTRACT	xxvi
CHAPTER 1 : INTRODUCTION	
1.0 Overview	1
1.1 Background to the III-Nitride Growth	3
1.2 Background to the Influential Parameters on III-Nitrides	6
1.3 Background to the Semiconductor Devices Simulation	7
1.4 Objectives of the Study	9
1.5 Originality of the Study	10
1.6 Outlines of the Study	10
CHAPTER 2: LITERATURE REVIEW AND THEORETICAL BACKGROUND	
2.0 Introduction	12
2.1 Growth Techniques of III-Nitride Group	12
2.1.1 Metal-Organic Chemical Vapour Deposition (MOCVD)	13
2.1.2 Halide Vapor Phase Epitaxy (HVPE)	15
2.1.3 Molecular Beam Epitaxy (MBE)	17
2.2 Growth of AlGaN Ternary Alloys	20
2.2.1 Influential Parameters in AlGaN Film Quality	21
2.2.1.1 Substrates Parameter	21

2.2.1.2	Buffer layers	23
2.2.2	Doping $\text{Al}_x\text{Ga}_{1-x}\text{N}$ Alloys	24
2.2.2.1	n-type Doping	25
2.2.2.2	p-type Doping	26
2.3	AlGaN/GaN Heterostructures	27
2.4	Metal-Semiconductor Contacts Theory	29
2.4.1	Ohmic Contact	30
2.4.2	Determination of Specific Contact Resistivity	32
2.4.3	Schottky Contact	33
2.4.4	Schottky Barrier Height	34
2.5	Principles of AlGaN-based Devices	36
2.5.1	AlGaN-Based Photodetector Device	36
2.5.1.1	Photoconductor	37
2.5.1.2	PIN Photodiode	38
2.5.1.3	Metal-Semiconductor-Metal (MSM) Photodiode	39
2.5.2	Measuring Responsivity of the Photodetectors	40
2.5.3	AlGaN-Based HEMT Device	40

CHAPTER 3: EXPERIMENTAL EQUIPMENT AND SIMULATION SOFTWARE

3.0	Introduction	44
3.1	MBE System	44
3.1.1	Load Lock Chamber	45
3.1.2	Buffer Chamber	45
3.1.3	Growth Chamber	46
3.1.3.1	Effusion Cells	46
3.1.3.2	Continuous Azimuthal Rotation (CAR)	49
3.1.3.3	Reflection High Energy Electron Diffraction (RHEED)	50
3.1.3.4	Pumps	52
3.1.4	Radio Frequency Plasma Nitrogen Sources	52

3.2	Mechanisms of MBE Film Growth	53
3.3	Principles of the Characterization Tools	55
3.3.1	The Structural Tools	55
3.3.1.1	X -ray diffraction (XRD)	56
3.3.1.2	Scanning Electron Microscopy (SEM)	58
3.3.1.3	Transmission Electron Microscopy (TEM)	60
3.3.1.4	Energy Dispersive X-rays Analysis (EDX)	61
3.3.1.5	Atomic Force Microscopy (AFM)	62
3.3.2	The Optical Tools	64
3.3.2.1	Photoluminescence Spectroscopy (PL)	64
3.3.2.2	Raman Spectroscopy	66
3.3.2.3	Optical Reflectometer	67
3.3.3	The Electrical Tools	68
3.3.3.1	Hall Effect	68
3.3.3.2	Current-Voltage Equipment	72
3.4	Metal Coating Tools	73
3.4.1	Sputtering System	73
3.4.2	Thermal Evaporator System	74
3.5	Thermal Annealing Processes	75
3.6	Simulation Software	76
3.6.1	Device Simulation Software	76
3.6.2	Device Structure	76
3.6.3	Device Simulator	78
3.6.3.1	Poisson's Equation	78
3.6.3.2	Continuity Equations	79
3.6.4	Simulation Models	79
3.6.4.1	Transport Models	80
3.6.4.2	Recombination Models	81

3.6.4.3	Band Structure	81
3.6.4.4	Mobility Models	82
3.6.4.5	Carrier Statistics Model	84
CHAPTER 4: METHODOLOGY		
4.0	Introduction	85
4.1	AlGa _x N Growth Procedures	85
4.1.1	Silicon Substrate Preparation	85
4.1.2	Substrate Outgassing Process	88
4.2	Material Sources and Growth Parameter Conditions	89
4.2.1	Ga Cleaning Process	90
4.2.2	Buffer Layer Deposition	91
4.2.3	GaN Layer Deposition	92
4.2.4	AlGa _x N Growth Layers	92
4.2.4.1	Undoped Al _x Ga _{1-x} N/GaN/AlN on Si(111) Substrate	92
4.2.4.2	n-type Al _{0.25} Ga _{0.75} N/GaN/AlN on Si(111) Substrate	93
4.3	Characterization of Al _x Ga _{1-x} N Samples	94
4.4	Studying Au, Pt and Ni as Metal Contacts on Device Structures	95
4.5	Fabrication and Characterization of Al _x Ga _{1-x} N-based Devices	96
4.5.1	Fabrication of Al _x Ga _{1-x} N-based MSM Photodetector Device	96
4.5.1.1	Characterization of Al _x Ga _{1-x} N MSM Photodetector	97
4.5.2	Fabrication of Al _x Ga _{1-x} N-based-HEMT Transistor Device	98
4.5.2.1	Al _x Ga _{1-x} N Wafer Cleaning	98
4.5.2.2	Optical Lithography	99
4.5.2.3	Mask Design	100
4.5.2.4	Procedures of the Photolithographic Process	101
4.5.2.5	Physical Metal Deposition for HEMT Transistor	103
4.5.2.6	Characterization of Al _x Ga _{1-x} N HEMT Transistor	105

CHAPTER 5: RESULTS AND DISCUSSION (Part I): STRUCTURAL, OPTICAL AND ELECTRICAL CHARACTERIZATIONS OF $\text{Al}_x\text{Ga}_{1-x}\text{N}$ THIN FILMS GROWN ON SILICON SUBSTRATE

5.0	Introduction	107
5.1	The Results of Undoped $\text{Al}_x\text{Ga}_{1-x}\text{N}$ Samples	107
5.1.1	RHEED	107
5.1.2	Scanning Electron Microscopy and Energy Dispersive X-ray Analysis	111
5.1.3	Atomic Force Microscopy (AFM)	113
5.1.4	X-ray Diffraction	114
5.1.5	Photoluminescence Measurements	118
5.1.6	Raman Measurements	119
5.1.7	Hall Effect Measurements	120
5.2	The Results of High Al-content $\text{Al}_x\text{Ga}_{1-x}\text{N}$ Sample	121
5.2.1	RHEED	121
5.2.2	Transmission Electron Microscopy and Energy Dispersive X-ray Analysis	122
5.2.3	Scanning Electron Microscopy (SEM)	124
5.2.4	Atomic Force Microscopy (AFM)	124
5.2.5	X-ray Diffraction	125
5.2.6	Photoluminescence Measurements	126
5.2.7	Raman Measurements	127
5.2.8	Hall Effect Measurements	128
5.3	Characterizations of n-type Si-doped $\text{Al}_x\text{Ga}_{1-x}\text{N}$ Sample	128
5.3.1	RHEED	129
5.3.2	Scanning Electron Microscopy and Energy Dispersive X-ray Analysis	130
5.3.3	Atomic Force Microscopy (AFM)	131
5.3.4	X-ray Diffraction	131
5.3.5	Photoluminescence Measurements	133
5.3.6	Raman Measurements	134

5.3.7	Hall Effect Measurements	134
5.4	The Effect of Al-mole Fractions on the Strain	135
5.5	Summary	137

CHAPTER 6: RESULTS AND DISCUSSION (Part II): METAL CONTACTS

6.0	Introduction	138
6.1	Ti/Al-based Ohmic Contacts on $\text{Al}_x\text{Ga}_{1-x}\text{N}$	138
6.2	Au- and Pt-based Schottky Contacts on $\text{Al}_x\text{Ga}_{1-x}\text{N}$	141
6.2.1	Scanning Electron Microscopy of Au and Pt-based Schottky Contact	141
6.2.2	Electrical Measurements of Au and Pt-based Schottky Contact	143
6.3	The Effect of Varying the Al-mole Fractions on Schottky Barrier Height	148
6.4	Summary	150

CHAPTER 7: RESULTS AND DISCUSSION (Part III): EXPERIMENTAL AND SIMULATION RESULTS OF $\text{Al}_x\text{Ga}_{1-x}\text{N}$ DEVICES

7.0	Introduction	151
7.1	AlGa _N Metal-Semiconductor-Metal (MSM) Photodetectors	151
7.1.1	UV Photodetectors Based on $\text{Al}_x\text{Ga}_{1-x}\text{N}$ Samples	152
7.1.2	Current-Voltage Measurements	152
7.1.3	Spectral Responsivity Measurements	153
7.2	AlGa _N /Ga _N High Electron Mobility Transistor (HEMT)	156
7.2.1	Physics-based Modeling of AlGa _N HEMTs	156
7.2.2	Experimental and Simulation Results of $\text{Al}_x\text{Ga}_{1-x}\text{N}$ based-HEMTs Device	163
7.3	Summary	170

CHAPTER 8: CONCLUSIONS AND FUTURE WORK

8.0	Overview	172
8.1	Conclusions	172

8.2	Future work	174
	REFERENCES	176
	APPENDICES	194
	APPENDIX A: Properties of AlGaN/GaN Heterostructures	195
	APPENDIX B: Simulation Parameters	199
	APPENDIX C: MBE Standby Condition	201
	APPENDIX D: Command Simulation Software	202
	PUBLICATIONS LIST	206

LIST OF TABLES

Table 2.1	Lattice constants, thermal expansion and lattice mismatch of substrates (Jain et al., 2000; Hanser et al., 1999; Vaillant et al., 1997)	21
Table 2.2	Electrical nature of ideal MS contacts	30
Table 4.1	Outgassing procedures of silicon substrate with different temperatures of chambers and time allocated	89
Table 4.2	Parameters condition for growth of III-nitride epilayers	90
Table 5.1	Growth rate as a function of thickness and growth time for Samples A, B and C	112
Table 5.2	The 2θ peak positions of $\text{Al}_x\text{Ga}_{1-x}\text{N}/\text{GaN}/\text{AlN}$ layers grown on Si (111) substrates for Samples A, B and C	115
Table 5.3	XRD results of $\text{Al}_x\text{Ga}_{1-x}\text{N}/\text{GaN}/\text{AlN}$ layers grown on Si (111) substrates for Samples A, B and C	117
Table 5.4	Optical phonon modes (in cm^{-1}) of $\text{Al}_x\text{Ga}_{1-x}\text{N}$ thin films grown on Si substrate for Samples A, B and C	120
Table 5.5	Hall effect measurement of unintentionally doped n-type $\text{Al}_x\text{Ga}_{1-x}\text{N}$ thin films grown on Si substrate	121
Table 5.6	The grain size and strain extracted from XRD measurements	136
Table 6.1	The specific contact resistivities of the unintentionally doped $\text{Al}_x\text{Ga}_{1-x}\text{N}$ (Sample B) with different annealing temperatures and times	140
Table 6.2	The specific contact resistivities of the Si-doped $\text{Al}_x\text{Ga}_{1-x}\text{N}$ (Sample E) with different annealing temperatures and times	141
Table 6.3	SBH for Au and Pt metal contacts on the unintentionally doped and Si-doped samples with different annealing temperatures	146
Table 6.4	The structural and electrical properties of $\text{Al}_x\text{Ga}_{1-x}\text{N}$ thin films	148
Table 7.1	The SBHs, n , dark and photo current of Samples B, C and D	152
Table 7.2	$I_{\text{DS,sat}}$ and g_m simulation and experimental results for Samples I and II	159
Table 7.3	Important lateral dimensions of unintentionally doped and Si-doped $\text{Al}_x\text{Ga}_{1-x}\text{N}$ HEMT structure	165
Table 7.4	Trap specifications used in the simulation software	166

LIST OF FIGURES

Figure 1.1	Band gaps of the most important semiconductors versus their lattice constant [adopted from Christian, (2010)].	2
Figure 2.1	The schematic diagram of a typical MOCVD growth reactor [adopted from Morkoc (1999)].	14
Figure 2.2	Schematic illustration for GaN HVPE growth: 1. main reactor tube, 2. heating elements, 3. Ga source gas channel, 4. boat with Ga melt, 5. Ga melt, 6. substrate, 7. substrate holder, and 8. ammonia source tube [adopted from Molnar (1998)].	16
Figure 2.3	Schematic diagram of MBE system for the deposition of III-V semiconductor compounds [adopted from Cho (1983)].	19
Figure 2.4	RF plasma source for producing nitrogen atoms [adopted from Hoke et al., (1991)].	20
Figure 2.5	Energy band gap diagram for wide (II) and narrow (I) band gap semiconductor [adopted from Sze, (1999)].	27
Figure 2.6	AlGa _N /Ga _N based structures with Ga-polarity. Polarization induced sheet charge density with direction of the spontaneous and the piezoelectric polarization (left); electron accumulation and formation of 2DEG at the interface (right).	28
Figure 2.7	Energy band diagrams for ideal MS contacts between a metal and an n-type semiconductor under equilibrium condition. [adopted from Sze, (1999)].	30
Figure 2.8	(a) Rectangular TLM pattern and (b) plot showing the variation of the resistance with respect to the gap distance. [adopted from Morkoc, (1999)].	32
Figure 2.9	The thermal equilibrium energy band diagram of a metal and semiconductor [adopted from Yu and Manasreh (2003)].	34
Figure 2.10	Plot of $\ln I$ as a function of V .	35
Figure 2.11	Schematic structure of the different types of AlGa _N photodetectors [adopted from Monroy et al., (2001)]	37
Figure 2.12	Schematic structure of a photoconductor.	38
Figure 2.13	Schematic structure of a PIN photodetector.	38

Figure 2.14	MSM photodetector consists of two contacts with interdigitated finger electrodes. Light incident on the semiconductor surface causes a photocurrent to flow between the biased contacts [adopted from Noriega, (2006)].	39
Figure 2.15	Schematic diagram of AlGa _N /Ga _N HEMT devices.	41
Figure 2.16	Band scheme of AlGa _N /Ga _N HEMT devices at zero gate voltage (left) and at negative gate voltage (right).	43
Figure 3.1	Veeco Gen II molecular beam epitaxy (MBE) system.	45
Figure 3.2	Effusion cells port location on source flange (viewed from rear side) [adopted from Veeco GEN II MBE system, Manual (2005)].	48
Figure 3.3	The schematic diagram of the RHEED system.	50
Figure 3.4	The RHEED diffraction pattern during growth process (a) two-dimensional diffraction and (b) three-dimensional diffraction.	51
Figure 3.5	Illustration of the RHEED specular spot oscillation depending on the surface morphology during monolayer growth [adopted from Ohring (1992)].	52
Figure 3.6	A typical radio-frequency (RF) sputtering system [adopted from Williams (1996)].	53
Figure 3.7	Schematic illustration of the surface processes during growth in a MBE system [adopted from Herman and Sitter (1996)].	54
Figure 3.8	Schematic diagram of the three distinct growth modes: Frank-van der Merwe, Volmer-Weber, and Stranski-Krastanov growth [adopted from Eaglesham and Cerullo, (1990)].	55
Figure 3.9	High resolution X-ray diffraction system.	56
Figure 3.10	X-ray diffraction from two parallel atomic planes in a crystalline material [adopted from Callister, (1997)].	57
Figure 3.11	Schematic diagram of SEM system.	59
Figure 3.12	Scanning electron microscopy (SEM) system.	60
Figure 3.13	The schematic diagram of TEM system where the lensing system (4,7 and 8) focuses the beam on the specimen and then projects it onto the viewing screen (10). The beam control is on right (13 and 14). [adopted from Fultz and Howe, (2007)].	61
Figure 3.14	Schematic diagram of the emission of X-ray [adopted from manual of Thermo Scientific].	62

Figure 3.15	A schematic diagram of the operation of an AFM [adopted from operating manual, surface imaging system (1999)].	63
Figure 3.16	PL and Raman spectroscopy system.	65
Figure 3.17	A schematic diagram of a typical PL setup.	66
Figure 3.18	Filmetrics system model (F20).	68
Figure 3.19	Hall effect measurement system.	69
Figure 3.20	A scheme of Hall effect in a bar of semiconductor with four ohmic contacts. The direction of the magnetic field B is along the z -axis; the sample has a finite thickness.	70
Figure 3.21	A schematic diagram of a Van der Pauw configuration used to determine the Hall voltage V_H .	71
Figure 3.22	A schematic diagram of a Van der Pauw configuration used to determine the two characteristic resistances R_A and R_B [adopted from Rietveld et al., (2003)].	72
Figure 3.23	Current-voltage system.	73
Figure 3.24	A schematic diagram of (a) sputtering chamber and (b) Edwards A500 RF magnetron sputtering system.	74
Figure 3.25	Thermal evaporator system.	75
Figure 3.26	Thermal annealing furnace system.	75
Figure 3.27	ISE tools flow [DESSIS ISE TCAD Manual, (2004)].	77
Figure 4.1	Installation of the substrate into the UNI-Block.	87
Figure 4.2	The UNI-Blocks on the trolley.	88
Figure 4.3	RHEED pattern of Si(111) 7x7 surface reconstruction pattern.	91
Figure 4.4	(a) A schematic diagram of the interdigitated Schottky contacts for MSM UV photodetector (b) The fabricated device of AlGaN MSM UV photodetector.	97
Figure 4.5	A schematic cross-section of the typical set up of spectral response measurements of the $Al_xGa_{1-x}N$ based MSM UV photodetectors.	98
Figure 4.6	The transistor mask design used in this study.	100
Figure 4.7	Steps of the photolithographic process.	101

Figure 4.8	The photolithography processes (a) Source-drain optical measurement of the successful fabrication of the transistor structure on the photoresist from standard lithography (b) Gate structure of the transistor (c) the final contacts of the transistor structure.	102
Figure 4.9	A schematic diagram of the fabrication processes (a) Source-Drain contacts, (b) Gate contact.	105
Figure 5.1	RHEED patterns during Ga cleaning processes (a) 7×7 surface reconstruction at high temperature before Ga cleaning, (b) during Ga cleaning and (c) after Ga cleaning.	108
Figure 5.2	RHEED patterns during the growth of (a) Al high flux (b) AlN (shutter opened for 15 minutes) and (b) GaN (shutter opened for 20 minutes) and (d) AlGa _{1-x} N (Sample B) (shutter opened for 25 minutes).	110
Figure 5.3	SEM cross-section images of Al _x Ga _{1-x} N/GaN/AlN layers grown on Si (111) substrates for Samples A, B and C.	112
Figure 5.4	Scanning electron microscopy (SEM) images and typical EDX spectra of Al _x Ga _{1-x} N/GaN/AlN layers grown on Si (111) substrates for Samples A, B and C.	113
Figure 5.5	AFM images of Al _x Ga _{1-x} N/GaN/AlN layers grown on Si (111) substrates for Samples A, B and C.	114
Figure 5.6	XRD scans of Al _x Ga _{1-x} N/GaN/AlN layers grown on Si (111) substrates for Samples A, B and C taken from the (0002) diffraction plane and measured by the 2θ - ω scan mode.	115
Figure 5.7	XRD symmetric RC $\omega/2\theta$ scans of (0002) plane of Al _x Ga _{1-x} N/GaN/AlN layers grown on Si (111) substrates for Samples A, B and C.	117
Figure 5.8	PL spectra of Al _x Ga _{1-x} N samples. The scales of the vertical axis for Al _x Ga _{1-x} N sample have been adjusted to magnify the RC spectra.	118
Figure 5.9	Room-temperature Raman spectra of Al _x Ga _{1-x} N/GaN/AlN layers grown on Si (111) substrates for Samples A, B and C.	119
Figure 5.10	RHEED patterns during the growth of AlGa _{1-x} N layers with different growth time for Sample D (a) after 5 minutes, (b) after 10 minutes, (c) after 20 minutes and (d) after 30 minutes.	122
Figure 5.11	Sample D: (a) Transmission electron microscopy (TEM) cross-section and (b) Energy dispersive X-ray spectroscopy (EDS) of the Al _x Ga _{1-x} N/GaN/AlN layers grown on Si substrate.	123

Figure 5.12	SEM surface morphology of the $\text{Al}_x\text{Ga}_{1-x}\text{N} / \text{GaN}/\text{AlN}$ layers grown on Si (111) substrate for Sample D.	124
Figure 5.13	AFM image of $\text{Al}_x\text{Ga}_{1-x}\text{N}/\text{GaN}/\text{AlN}$ layers grown on Si (111) substrates for Sample D.	124
Figure 5.14	XRD scan of $\text{Al}_x\text{Ga}_{1-x}\text{N}/\text{GaN}/\text{AlN}$ layers grown on Si (111) substrates for Sample D taken from the (0002) diffraction plane and measured by the 2θ - ω scan mode.	125
Figure 5.15	XRD symmetric RC $\omega/2\theta$ scans of (0002) plane of $\text{Al}_x\text{Ga}_{1-x}\text{N}/\text{GaN}/\text{AlN}$ layers grown on Si (111) substrates for Sample D.	126
Figure 5.16	PL spectrum of $\text{Al}_x\text{Ga}_{1-x}\text{N}/\text{GaN}/\text{AlN}$ grown on Si substrate for Sample D.	127
Figure 5.17	Room temperature Raman spectrum of $\text{Al}_x\text{Ga}_{1-x}\text{N}/\text{GaN}/\text{AlN}$ grown on Si substrate for Sample D.	128
Figure 5.18	RHEED patterns during the growth of Sample E (a) Al pattern (opening the shutter for 15min), (b) Ga pattern (opening the shutter for 20 min and (c) AlGa _N pattern (opening the shutter for 25 min).	129
Figure 5.19	SEM cross-section of Si-doped $\text{Al}_x\text{Ga}_{1-x}\text{N}/\text{GaN}/\text{AlN}$ layers grown on Si (111) substrates for Sample E.	130
Figure 5.20	SEM surface morphology of the Si-doped AlGa _N /Ga _N /Al _N layers grown on Si(111) substrate for Sample E.	131
Figure 5.21	AFM surface image of the Si-doped AlGa _N /Ga _N /Al _N layers grown on Si(111) substrate for Sample E.	131
Figure 5.22	XRD spectrum of the Si-doped $\text{Al}_x\text{Ga}_{1-x}\text{N}$ taken from the (0002) diffraction plane and measured by the 2θ - ω scan mode for Sample E.	132
Figure 5.23	XRD symmetric RC ω scans of (0002) plane of the Si-doped $\text{Al}_x\text{Ga}_{1-x}\text{N}$ for Sample E.	133
Figure 5.24	PL spectrum of the Si-doped $\text{Al}_x\text{Ga}_{1-x}\text{N}/\text{GaN}/\text{AlN}$ grown on Si(111) substrate for Sample E.	133
Figure 5.25	Room-temperature Raman spectrum of Si-doped $\text{Al}_x\text{Ga}_{1-x}\text{N}/\text{GaN}/\text{AlN}$ grown on Si(111) substrate for Sample E.	134
Figure 5.26	The plot of grain size vs the strain ϵ_{zz} (%) along c axis of $\text{Al}_x\text{Ga}_{1-x}\text{N}$ samples.	136

Figure 6.1	SEM images of Au-based metal contact onto $\text{Al}_x\text{Ga}_{1-x}\text{N}$ with different annealing temperatures (a) unintentionally doped sample and (b) Si-doped sample.	142
Figure 6.2	SEM images of Pt-based metal contact onto $\text{Al}_x\text{Ga}_{1-x}\text{N}$ with different annealing temperatures (a) unintentionally doped sample and (b) Si-doped sample.	143
Figure 6.3	Plot of voltage as a function of $\ln I$ to calculate the barrier height for Pt contact on n-type $\text{Al}_{0.25}\text{Ga}_{0.75}\text{N}$ at annealing temperature 600 °C (inset figure to find slope of line and y-intercept using equation 2.7).	144
Figure 6.4	The I - V characteristics of Au-Schottky contact with different annealing temperatures (a) unintentionally doped n-type $\text{Al}_x\text{Ga}_{1-x}\text{N}$ (Samples B) and (b) Si-doped $\text{Al}_x\text{Ga}_{1-x}\text{N}$ (Sample E).	145
Figure 6.5	The I - V characteristics of Pt-Schottky contact with different annealing temperatures (a) unintentionally doped $\text{Al}_x\text{Ga}_{1-x}\text{N}$ (Samples B) and (b) Si-doped $\text{Al}_x\text{Ga}_{1-x}\text{N}$ (Sample E).	147
Figure 6.6	The I - V characteristics of the $\text{Al}_x\text{Ga}_{1-x}\text{N}$ samples with Ni Schottky contacts.	149
Figure 6.7	The Al-mole fractions of $\text{Al}_x\text{Ga}_{1-x}\text{N}$ samples as a function of the Ni Schottky barrier height.	150
Figure 7.1	The I - V characteristics of $\text{Al}_x\text{Ga}_{1-x}\text{N}$ samples of MSM UV photodetectors for (a) Sample B, (b) Sample C and (c) Sample D.	154
Figure 7.2	The responsivity of $\text{Al}_x\text{Ga}_{1-x}\text{N}$ as a function of wavelength for MSM UV photodetectors for (a) Sample B, (b) Sample C and (c) Sample D.	155
Figure 7.3	Schematic structure of AlGaN/GaN (a) without Mg-doped layer (Sample I) and (b) with Mg-doped semi-insulating carrier confinement layer (Sample II) [Adopted from Chang et al., (2003)].	157
Figure 7.4	The output characterization of the drain-source current as a function of the drain-source voltage of Sample I.	158
Figure 7.5	Transconductance and drain-source current as a function of V_{GS} for Sample I.	159
Figure 7.6	The output characterization of the drain-source current as a function of the drain-source voltage of Sample II.	160
Figure 7.7	Transconductance and drain-source current as a function of V_{GS} for Sample II.	161

Figure 7.8	I_{DS} - V_{DS} characteristics as functions of the ambient temperature T at V_{GS} of 1.5 V for Sample I.	162
Figure 7.9	I_{DS} - V_{DS} characteristics as functions of the ambient temperature T at V_{GS} of 1.5 V for Sample II.	162
Figure 7.10	I_{DS} - V_{DS} characteristics as functions of the source and drain resistance (R_s, R_d) at V_G of 1.5 V for Sample I.	163
Figure 7.11	I_{DS} - V_{DS} characteristics as functions of the source and drain resistance (R_s, R_d) at V_G of 1.5 V for Sample II.	163
Figure 7.12	The typical structure of $Al_xGa_{1-x}N$ /GaN/AlN/Si HEMT device (a) unintentionally doped sample and (b) Si-doped sample.	164
Figure 7.13	The output characterization of I_{DS} - V_{DS} for the experimental and simulation results with gate voltage V_G swept from -8 to +2 V with step of 2 V (a) unintentionally doped sample and (b) Si-doped sample.	167
Figure 7.14	The experimental and simulation results of the drain current plotted with gate voltage at V_{DS} of 8 V (a) unintentionally doped sample and (b) Si-doped sample.	168
Figure 7.15	The experimental and simulation results of transconductance g_m plotted with gate voltage at V_{DS} of 8 V (a) unintentionally doped sample and (b) Si-doped sample.	170

LIST OF ABBREVIATIONS

III-V	Material, typically crystalline, composed of roughly equal parts of elements from group –III of the periodic table and elements from group-V of the periodic table
2D	Two-dimensional
2DEG	Two-dimensional electron gas
AFM	Atomic force microscopy
AlGaN	Aluminum gallium nitride
AlN	Aluminum nitride
BEP	Beam equivalent pressure
BFM	Beam flux monitor
CAR	Continuous azimuthal rotation
CCD	Charge-coupled device
CL	Cathodoluminescence
CRD	Cathode ray display
ECR	Electron cyclotron resonance
EDX	Energy dispersive X-ray
FET	Field effect transistors
FM	Frank-van der Merwe
FWHM	Full-width at half maximum
GaN	Gallium nitride
HEMT	High electron mobility transistors
HFET	Heterostructure field effect transistor
HRXRD	High resolution X-ray diffraction
HVPE	Halide vapor phase epitaxy
InGaN	Indium gallium nitride

InN	Indium nitride
ISE TCAD	Integrated System Engineering Technology Computer Aided Design
LD	Laser diode
LED	Light emitting diode
LEEBI	Low energy electron beam irradiation
MBE	Molecular beam epitaxy
MESFET	Metal semiconductor field effect transistor
MIS	Metal-Insulator-Semiconductor
MOCVD	Metal-organic chemical vapor deposition
MODFET	Modulation doped field effect transistor
MS	Metal-semiconductor
MSM	Metal-semiconductor-metal
N.O.R	Nano Optoelectronics Research and Technology
PBN	Pyrolytic boron nitride
PL	Photoluminescence
RC	Rocking curves
RCA	Radio Corporation of America
RF	Radio frequency
RHEED	Reflection high energy electron diffraction
RMS	Root mean square
SBH	Schottky barrier height
SEM	Scanning electron microscopy
SiN	Silicon nitride
SK	Stranski-Krastanov
TEGa	Triethylgallium
TLM	Transmission line method
TMAI	Trimethylaluminum

TMGa	Trimethylgallium
TMIn	Trimethylindium
UHV	Ultra-high vacuum
UID	Unintentionally doped
UV	Ultraviolet
V_N	Nitrogen vacancies
VW	Volmer-Weber
XRD	X-ray diffraction

LIST OF SYMBOLS

x	Al mole fraction
E_g	Energy band gap
ϵ	Electrical permittivity
χ	Electron affinity
ΔE_c	Discontinuity in the conduction band
ΔE_v	Discontinuity in the valence band
P_{PE}	Piezoelectric polarization
P_{sp}	Spontaneous polarization
E_F	Fermi level
ϕ_M	Metal work function
ϕ_S	Semiconductor work function
l_i	The spacing between two pads
R_{sh}	Sheet resistance
R_c	Resistance
L_t	Transfer length
W_C	Width of contact pad
ρ_c	Specific resistivity
Φ_B	Barrier height
V_0	Contact potential
I_o	Saturation current
n	Ideality factor
K	Boltzmann's constant
T	Absolute temperature
A	Area of contact
A^*	Effective Richardson coefficient

h	Planck's constant
m^*	Effective electron mass
m_0	Electron mass
q	Electron charge
n_s	Sheet carrier concentration of free electrons
μ	Mobility of the electrons
σ	Conductivity
L_G	Gate length
W_g	Gate width
D	Thickness of active layer
L_{GS}	Gate-source terminal spacing
L_{GD}	Gate-drain terminal spacing
$I_{DS, \text{sat}}$	Drain-source saturation current
g_m	Transconductance
I_{DS}	Drain-source current
V_G	Gate voltage
α	Optical absorption coefficient
λ	X-ray wavelength
d_{hkl}	The interplaner spacing of the diffraction planes
θ	Diffraction angle in degree
c	Lattice constant
R_H	Hall coefficient
B	Magnetic field
V_H	Hall voltage
ψ	Electrostatic potential
N_{D^+}	The number of the ionized donors per unit volume

N_A	The number of the ionized acceptors per unit volume
J_n	The total current density of electrons
J_p	The total current density of holes
G	The generation rate per unit volume
R	The net electron-hole recombination rate per unit volume
μ_n	Electron mobility
μ_p	Hole mobility
Φ_n	Electron quasi-Fermi potentials
Φ_p	Hole quasi-Fermi potentials
E_{trap}	Difference between the defect level and the intrinsic level
$E_g(0)$	Band gap energy at 0 K
β	Fitting parameter
N_C	Effective density of states at conduction band
N_V	Effective density of states at valence band
μ_L	Mobility due to the bulk phonon scattering
ξ	Fitting parameter
μ_{low}	Low field mobility
F	Driving field
v_{sat}	Saturation velocity
V_{DS}	Drain-source voltage
V_{GS}	Gate-source voltage
I_{DS}	Drain-source current
R_s	Source resistance
R_d	Drain resistance
L_s	Source contact length
L_d	Drain contact length

FILEM TIPIS AlGa_xN ATAS SUBSTRAT SILIKON UNTUK PERANTI PENGESAN CAHAYA DAN TRANSISTOR

ABSTRAK

Kajian ini menyelidiki aloi Al_xGa_{1-x}N yang ditumbuhkan atas substrat Si bagi aplikasi pengesan cahaya dan transistor. Teknik epitaksi alur molekul frekuensi radio (RF) nitrogen plasma-terbantu (PA-MBE) telah digunakan untuk menumbuhkan filem nipis Al_xGa_{1-x}N/GaN/AlN atas substrat Si(111). Sampel Al_xGa_{1-x}N yang tidak didop dan didop dengan Si jenis n dengan pecahan mol Al yang berbeza telah berjaya ditumbuhkan. Belauan elektron pantulan tenaga tinggi (RHEED), mikroskop imbasan elektron (SEM), mikroskop transmisi elektron (TEM), mikroskop daya atomik (AFM), belauan sinar-X resolusi tinggi (HR-XRD), fotoluminesen (PL), serakan Raman dan pengukuran kesan Hall telah digunakan untuk mengkaji pola rekonstruksi, keratan rentas, morfologi permukaan, kekasaran permukaan, pecahan mol, kualiti hablur dan kepekatan pembawa. Sampel Al_xGa_{1-x}N dengan pecahan mol Al yang tinggi dengan kualiti hablur yang baik telah berjaya ditumbuhkan di atas substrat Si. Pengukuran kesan Hall menunjukkan bahawa sampel jenis-n Al_{0.25}Ga_{0.75}N yang didop dengan Si mempunyai kepekatan pembawa yang tinggi iaitu $3.93 \times 10^{19} \text{ cm}^{-3}$.

Kesan terikan ke atas saiz butiran dengan pecahan mol Al yang berbeza bagi sampel Al_xGa_{1-x}N yang tidak didopkan telah dikaji. Keputusan struktur dan morfologi permukaan telah menunjukkan bahawa secara relatif terikan tegangan yang lebih besar wujud dalam sampel yang mempunyai pecahan mol Al yang terkecil; manakala terikan mampat yang lebih kecil dan saiz butiran yang lebih besar wujud dalam sampel yang mempunyai pecahan mol Al sebanyak 0.3. Terikan berkurangan bagi sampel yang mempunyai pecahan mol Al yang tertinggi iaitu 0.43.

Sentuhan ohmik dwilapisan Ti/Al pada sampel-sampel $\text{Al}_x\text{Ga}_{1-x}\text{N}$ yang tidak didop dan yang didop dengan Si jenis-n telah diterokai. Rintangan sentuhan spesifik bagi sentuhan ini adalah peka pada perubahan suhu dan masa sepuhlindap. Bagi sentuhan Schottky berasaskan Au dan Pt, keputusan menunjukkan bahawa sampel jenis-n yang didop dengan Si mempunyai ciri-ciri Schottky yang baik untuk kedua-dua sentuhan. Keputusan baik bagi ketinggian sawar Schottky (SBH) telah diperolehi bagi sampel yang disepuhlindap pada $600\text{ }^\circ\text{C}$. Bagi sentuhan Scottky berasaskan Ni, SBH yang tertinggi telah diperolehi bagi sampel dengan pecahan mol Al sebanyak 0.30.

Pengesan cahaya UV logam-semikonduktor-logam (MSM) sampel $\text{Al}_x\text{Ga}_{1-x}\text{N}$ ($x = 0.24, 0.30$ dan 0.43) telah dikajikan. Untuk semua sampel, nilai SBH dalam keadaan pencahayaan adalah lebih kecil yang diterjemahkan kepada arus yang lebih tinggi untuk pengesan cahaya. Keputusan sambutan menunjukkan bahawa dengan peningkatan pecahan mol Al, sambutan ditingkatkan, menunjukkan bahawa sampel-sampel mempunyai kualiti yang baik dengan pecahan mol Al yang tinggi.

Akhirnya, keputusan eksperimen dan simulasi transistor elektron mobiliti tinggi (HEMTs) berasaskan $\text{Al}_x\text{Ga}_{1-x}\text{N}$ ($x = 0.24, 0.25$) yang tidak didop dan didop dengan Si jenis-n telah diselidiki. Keputusan simulasi yang diperolehi dengan menggunakan perisian *Integrated System Engineering Technology Computer Aided Design* (ISE TCAD) adalah dalam persetujuan yang munasabah dengan keputusan eksperimen, dengan beberapa pengecualian.

AlGaN THIN FILMS ON SILICON SUBSTRATES FOR PHOTODETECTOR AND TRANSISTOR DEVICES

ABSTRACT

This study examined $\text{Al}_x\text{Ga}_{1-x}\text{N}$ alloys grown on Si substrate for UV photodetectors and transistors applications. Radio-frequency (RF) nitrogen plasma-assisted molecular beam epitaxy (PA-MBE) technique was used to grow $\text{Al}_x\text{Ga}_{1-x}\text{N}/\text{GaN}/\text{AlN}$ thin films on the Si(111) substrates. Undoped and n-type Si-doped samples of $\text{Al}_x\text{Ga}_{1-x}\text{N}$ with different Al-mole fractions were successfully grown. Reflection high energy electron diffraction (RHEED), scanning electron microscopy (SEM), transmission electron microscopy (TEM), atomic force microscopy (AFM), high-resolution X-ray diffraction (HR-XRD), photoluminescence (PL), Raman scattering and Hall effect measurements were used to investigate the reconstruction pattern, cross-section, surface morphology, surface roughness, mole fractions, crystalline quality and carrier concentration of the thin films. High Al-mole fractions of $\text{Al}_x\text{Ga}_{1-x}\text{N}$ samples with good crystal quality have successfully been grown on the Si(111) substrates. Hall effect measurements showed that n-type Si-doped $\text{Al}_{0.25}\text{Ga}_{0.75}\text{N}$ has high carrier concentration of $3.93 \times 10^{19} \text{ cm}^{-3}$.

The effect of strain on the grain size with different Al-mole fractions of undoped $\text{Al}_x\text{Ga}_{1-x}\text{N}$ samples has been investigated. The results of structural and surface morphology indicated that there is a relatively larger tensile strain in the sample with the smallest Al-mole fraction; while a smaller compressive strain and larger grain size appear with the Al-mole fraction of 0.30. The strain gets relaxed for the sample with the highest Al-mole fraction of 0.43. Ti/Al bi-layer ohmic contacts on undoped and n-type Si-doped $\text{Al}_x\text{Ga}_{1-x}\text{N}$ samples have been explored. The specific contact resistivities of this contact are sensitive to the change of annealing temperatures and annealing time as well as to the carrier concentration. For Au- and

Pt-based Schottky contacts, the results showed that the sample with n-type Si-doping exhibit good Schottky behavior for both contacts. Good results for Schottky barrier heights (SBHs) have been obtained for sample annealed at 600 °C. For Ni-based Schottky contacts, the findings revealed that the highest SBH has been obtained for the sample with the Al-mole fraction of 0.30.

Metal-semiconductor-metal (MSM) UV photodetectors of $\text{Al}_x\text{Ga}_{1-x}\text{N}$ ($x = 0.24, 0.30$ and 0.43) samples have been presented. For all of the samples, the SBHs under illumination conditions are smaller which are translated to higher current for the photodetectors. The responsivity results revealed that with increasing of the Al-mole fractions, the responsivity increases, indicating that the samples have good quality with high Al-mole fractions.

Finally, the experimental and simulation results of high electron mobility transistors (HEMTs) based on undoped and n-type doped $\text{Al}_x\text{Ga}_{1-x}\text{N}$ ($x = 0.24, 0.25$) samples have been investigated. The simulation results obtained using Integrated System Engineering Technology Computer Aided Design (ISE TCAD) software are in reasonable agreement with the experimental results, with few exceptions.

CHAPTER 1

INTRODUCTION

1.0 Overview

Owing to their large band gap and excellent optical and electrical properties for the III-V nitride materials which include gallium nitride (GaN), aluminum nitride (AlN) and indium nitride (InN), their alloys and heterostructures such as AlGa_xN/GaN and InGa_xN/GaN have attracted many researches worldwide. The materials based on III-nitride group are suitable for fabricating devices such as sensors, radar, satellite, wireless base stations, photodetectors and high electron mobility transistors (HEMTs) which operate at high temperatures and in hostile environments. These devices are by far the best investigated III-nitrides group electronic devices (Anderson et al., 2008; Molnar et al., 1995; Jain et al., 2000; Chen et al., 1999; Kim and Jin, 2003).

III-nitride materials and AlGa_xN ternary alloys are one of the most promising materials which have been used as potentials for different applications in semiconductor light emitting devices, electron field effect transistors as well as solar-blind ultraviolet (UV) detectors, particularly for operating under hostile condition (Khan et al., 1995; Wu et al., 1996; Khan et al., 1996a; Wu et al., 1998).

Moreover, the direct and wide band gap energy that ranges from 3.4 eV for GaN and 6.2 eV for AlN, means that Al_xGa_{1-x}N materials are suitable candidates for ultraviolet (UV) part of the spectrum and solar-blind photodetectors (Kim and Jin, 2003; Averine et al., 2008). Figure 1.1 shows the band gap and lattice constant of some important compound semiconductor materials.

In addition, the excellent electrical properties of these materials such as high thermal conductivity, high breakdown fields, high peak velocity and high saturation velocity make these materials appropriate for the applications in both optoelectronic and electrical devices.

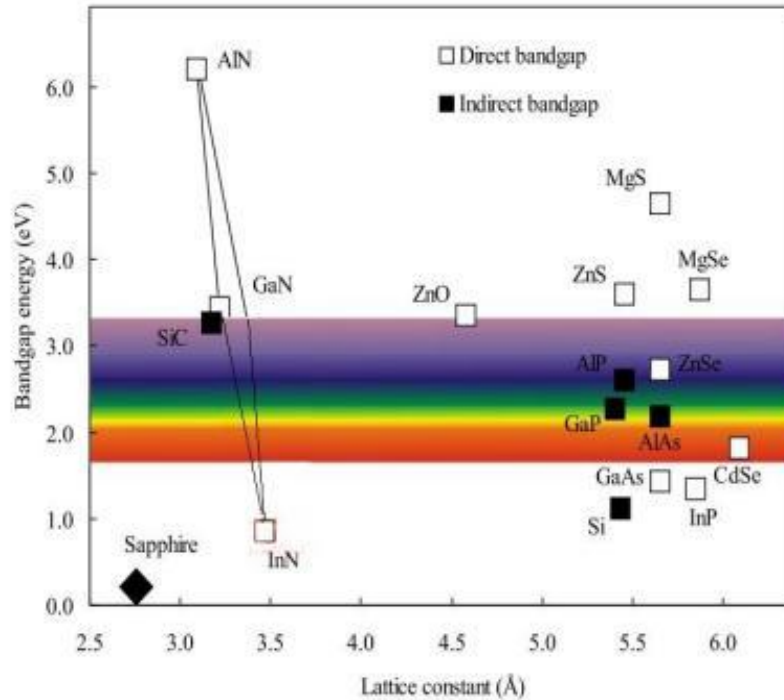


Figure 1.1: Band gaps of the most important semiconductors versus their lattice constant [adopted from Christian, (2010)].

Polarity also plays an important role as it contributes to growth of good quality of III-nitride materials. Unlike other III-V compounds, nitride-based epitaxial layers exhibit wurtzite crystal structure (Kuo et al., 2002; Chen et al., 2001; Lai et al., 2001; Ambacher et al., 1998; Kozodoy et al., 1999; Rashmi et al., 2002). The wurtzite crystal structure also results in a much larger piezoelectric field in nitride-based heterostructures compared to other III-V compounds (Ambacher et al., 2000; Bykhovski et al., 1993). For AlGa_n/Ga_n HFETs, it has been shown that piezoelectric polarization of the strained AlGa_n barrier plays an important role in the

performance of such devices (Kozodoy et al., 1999; Rashmi et al., 2002). The properties of AlGaN/GaN heterostructures are summarized in Appendix A.

To achieve high-performance HFETs, increasing of the two-dimensional electron gas (2DEG) density and the carrier mobility in the channel is needed. For the large 2DEG density, it can simply be done by increasing the Al mole fraction of the $\text{Al}_x\text{Ga}_{1-x}\text{N}$ layer because most carriers are induced by the piezoelectric polarization of the strained AlGaN barrier. An $\text{Al}_x\text{Ga}_{1-x}\text{N}$ barrier with a large Al mole fraction also provides a large conduction band discontinuity and a high Schottky barrier height where both of which can enhance the device performance. The increasing Al-content in AlGaN alloy is another challenge that many researchers have been attempting to obtain good quality samples with high Al-mole fraction in these alloys (Hwang et al., 2002).

1.1 Background to the III-nitride Group Growth

The attempts to synthesize III-nitride compounds were made relatively earlier in 1938 when Juza et al. (1938) obtained small GaN needles by passing ammonia over gallium. In late 1969, the first GaN films over large area were grown using chemical vapor deposition on a sapphire substrate (Maruska and Tietjen, 1969). However, all of the GaN samples at that time suffered from high free electron concentrations owing to large background doping mostly associated to nitrogen vacancies and silicon or oxygen impurities in the epitaxial layers (Pankove, 1997). In spite of these samples were of poor quality, researchers successfully fabricated the first light emitting diode (LEDs) with a GaN:Zn/n-GaN metal insulating semiconductor (MIS) diode (Pankove et al., 1972). After that, GaN epitaxial layers

of good quality were obtained in 1983 by Youshida, Misawa and Gonda using a two-step growth technique.

In fact, this technique has so far resulted in remarkable improvement to the material quality when a low-temperature AlN buffer layer is grown between the substrate and the high-temperature GaN layer. This makes the buffer layer become part of the growth process which leads to improvement of the film quality by reducing the mismatch between the substrate and main epitaxial layer. Subsequently, in 1988, the improvement in the two-step technique resulted in an optimum thickness and temperature for the grown AlN buffer layer (Amano et al., 1988). In addition, the interest in nitride-based materials has increased rapidly when Amano, Kito, Hiramatsu, and Akasaki, (1989) presented the successful growth of p-type GaN. They found that the high resistance of magnesium (Mg) doped GaN reduced greatly and that the cathodoluminescence (CL) significantly increased when the samples were irradiated by the electrons. They showed that p-type conduction could be obtained by low energy electron beam irradiation (LEEBI). This amazing finding was explained by Vechten, Zook, and Horning, (1992). They suggested that high resistivity of GaN:Mg was due to Mg:H which was broken with the electron beams. In the same year, Nakamura et al. (1992), found out that the Mg acceptors can be activated through thermal annealing of GaN:Mg film at temperatures above 750 °C with nitrogen.

On the other hand, improvement in nitride material quality resulted from development of ternary alloys that are essential in fabricating efficient devices. The first investigation of growth of AlGaN alloys was carried out by Khan, Skogman, and Hove, (1990), and InGaN alloys by Nakamura et al. (1993). This has led to

improvement for the semiconductor industry of LEDs, laser diode (LDs) and power transistors.

The development in growth technology of the nitride semiconductors, has promoted a number of researchers to fabricate different devices. In 1989, Amano et al. (1989), fabricated the first GaN p-n junction LED. Then, Khan et al. (1992), designed the first GaN UV photodetectors. After that, in 1993, Khan et al. (1993) presented the first nitride-based field effect transistors (FET). The first breakthrough of AlGaN/GaN high electron mobility transistors (HEMTs) was demonstrated by Khan et al. (1994). Later, Wu et al. (1995), reported the first power data for AlGaN/GaN HEMTs with 30 nm $\text{Al}_{0.15}\text{Ga}_{0.85}\text{N}$ on a thin film buffer (0.3 μm) on a sapphire substrate. The important development in nitride-related technology was made by Nakamura et al. (1996), who reported the first nitride LD. Recently, higher output characteristics for GaN-based devices have been achieved due to the improvements to the material quality and device processing (Micovic et al., 2000). High performance of AlGaN/GaN HEMT on the sapphire substrate has been examined (Kumar et al., 2002).

More recently, many techniques have been used to grow III-nitride materials such as halide vapor phase epitaxy (HVPE), metal-organic chemical vapor deposition (MOCVD), and molecular beam epitaxy (MBE). III-nitride materials have been used in different applications such as UV photodetectors and high electron mobility transistors (Ahn et al., 2005; Tsukihara et al., 2007; Wu et al., 2004; Yu and Manasreh, 2003) with varied performance.

1.2 Background to the Influential Parameters on III-nitride Group

The major difficulty of growing good quality III-nitride group materials is the lack of a suitable substrate material that is lattice-matched and thermally compatible with AlGaIn/GaN heterostructure. The binary and ternary alloys are mostly grown on silicon (Si) and sapphire (Al_2O_3) substrates because these substrates have some advantages; they are of low cost, available, transparent and stable at high temperature (Jain et al., 2000). Moreover, Si is a very attractive substrate for GaN epitaxy and offers large area wafers at a low cost with a good thermal conductivity (1.5 W/cmK). However, Si has a large lattice mismatch (about 17%) and a high thermal expansion coefficient mismatch, which results in a crack on the surface. However, the lattice mismatch of GaN epitaxy with sapphire substrate is equal to (16.1%), which indicates that the growth with Si substrate causes more cracks and dislocation density than sapphire substrate (Jothilingam et al., 2001).

To overcome the problem of lattice mismatch, buffer layer is used to decrease the mismatch and improve the quality between AlGaIn/GaN heterostructure and the substrate. However, the AlN binary material has a lattice mismatch equal to (13.2%); therefore, this material is used as a buffer layer to reduce the mismatch between epitaxial layers (Amano et al., 1986).

The two important parameters for highly controlled growth of III-nitride group epilayer are the nitrogen ratio and the growth temperature. It was found that changing of the growth temperature or the ratio of V/III could cause great influences on crystalline quality of the material (Jain et al., 2000).

Doping of III-nitride materials is also required to realize many types of devices. For example, the cladding layers which surround the active region of a III-nitride laser diode, are usually either n-type or p-type AlGaIn of higher Al mole

fraction to achieve transmission of shorter wavelength (Yu and Manasreh, 2003). Similar cladding layers were used for UV photodetectors. Modulation doping of AlGaIn/GaN HEMTs is sometimes employed by using a Si-doped layer of AlGaIn near the desired 2DEG channel to obtain excellent high-frequency characteristics (Khan et al., 1996). Unintentional n-type conduction for $\text{Al}_x\text{Ga}_{1-x}\text{N}$ alloys is well-documented; this behavior has been attributed to either nitrogen vacancies (V_N) or impurities such as oxygen (Perlin et al., 1995). However, it has recently been shown that the V_N formation energy is high for n-type GaN and AlN; therefore, nitrogen vacancies cannot be formed in a high concentration (Stampfl and Walle, 2002). A recent study conducted by Nepal et al. (2004), showed that V_N in AlN has a large donor binding energy (260-300 meV) and hence it would not make a significant contribution to n-type doping of AlN.

1.3 Background to the Semiconductor Devices Simulation

The advantage of the semiconductor device simulation is that the device can be studied and optimized using commercially available software instead of fabricating experimentally. This considerably saves the cost of development and time required to find the best device performance compared with fabrication of the devices. Subsequent work will be done experimentally to determine the best performance and device design, and this leads to accurate device modeling. To simulate the device accurately, the material properties must be known as well as the incorporation of the important relevant material physics. Because the use of AlGaIn and GaN semiconductors is relatively new compared to other semiconductors such as silicon, some of their material properties are not well known. Properties of these materials can be known through carrying out a number of experimental results.

Within this context, some researchers have been developing new methods to grow higher quality AlGa_N and GaN with fewer defects. A number of researchers have reported some successful modeling of AlGa_N/GaN HEMTs. Sacconi et al. (2001) have modeled the devices based on the self-consistent solution of the Schrodinger and Poisson equations when coupled to a quasi-2D model with current flow. On the other hand, Vetury et al. (2001) have proposed a model that is based upon electron injection from the metal to the surface states between the gate and the drain to explain the observed current collapse.

Sahoo et al. (2003), have also proposed an electron leakage model from the 2D channel to the surface states as a possible mechanism to explain the role of the surface states. Moreover, this simulation model was performed in the absence of any surface states. Braga et al. (2004), showed the importance of using the hydrodynamic transport model into the device simulation to account for the negative differential conductance in the output characteristics observed experimentally. The researcher has noticed that these scholars have used the commercially available device simulation software Integrated System Engineering Technology Computer Aided Design (ISE TCAD) to carry out their 2D numerical calculations.

ISE TCAD software simulation has been used to explain the relationship between breakdown voltage and gate leakage current together with the effect of field plates (Saito et al., 2005a; Saito et al., 2005b). ATLAS software is also another commercial device simulator which has successfully been used to investigate GaN-based device performance to explain the effect of the field plate on the breakdown voltage (Karmalkar and Mishra, 2001).

1.4 Objectives of the Study

The main objective of this research is to focus on the growth of $\text{Al}_x\text{Ga}_{1-x}\text{N}$ on Si(111) substrate using plasma-assisted molecular beam epitaxy (PA-MBE) technique with various composition (in particular high Al-mole fraction x) material to obtain a heterostructure with high quality. A high Al-mole fraction of $\text{Al}_x\text{Ga}_{1-x}\text{N}$ with good crystalline quality is necessary to increase the optical and electrical properties of semiconductors such as, the two-dimensional gas (2-DEG) density, carrier mobility, large conduction band discontinuity and high Schottky barrier height. These properties can enhance the devices performance. However, in this study, it is very important to study the parameters that may affect the growth kinetics which is necessary to obtain the $\text{Al}_x\text{Ga}_{1-x}\text{N}/\text{GaN}/\text{AlN}$ heterostructure on the Si substrate. In order to study the growth kinetics, the accurate determinations of growth parameters are crucial such as the surface temperature and material fluxes.

The second objective is to study the effect of the strain on the $\text{Al}_x\text{Ga}_{1-x}\text{N}$ samples with different Al-mole fractions to obtain information about the type of strain exhibited (compressive or tensile) and also to see the effect the strain on the structural and electrical properties of the samples.

The third objective is to study metal contacts on the undoped and n-type Si-doped AlGa_N-based materials for investigation of the effect of different types of the contacts material on the electrical properties. This study is to enhance the device performance. The growth process of the target materials and deposition of suitable contacts to fabricate the target device (MSM photodetector and HEMT) based on AlGa_N heterostructure are investigated.

The fourth objective is to fabricate the metal-semiconductor-metal (MSM) UV photodetectors based on AlGa_N/Ga_N materials to examine the range of the

working wavelength of these materials and HEMT structure. As such, the simulation results obtained by using ISE TCAD software will be compared with the experimental result to better understand the underlying physics of the carrier kinetics in III-nitride heterostructures and also to optimize the structure design.

1.5 Originality of the Study

The originality of this study includes firstly, high Al-content of $\text{Al}_x\text{Ga}_{1-x}\text{N}$ epilayers on low cost Si (111) substrates has successfully been grown by radio frequency (RF) nitrogen plasma-assisted molecular beam epitaxy (PAMBE) with good crystalline quality. Secondly, a good quality n-type Si-doped AlGaN on Si (111) substrate with high carrier concentration has been obtained. Thirdly, the metal-semiconductor-metal (MSM) photodetectors which work in deep UV range have been fabricated. Finally, a new application of experimental and simulated HEMTs transistors of AlGaN/GaN/AlN/Si material has been introduced.

1.6 Outlines of the Study

Chapter One describes the background of growth and the development of III-nitride materials and its applications for some optoelectronic devices.

Chapter Two explains the relevant theories to conduct this study. This includes the theory of growth techniques of III-nitride group, theory of metal contacts technology and the relevant concepts of ohmic and Schottky contacts. Theories of development of the AlGaN-based devices are also used.

Chapter Three covers the salient properties of a typical MBE system. After that, the characterization tools that provide information about the structural, optical

and electrical properties are also described. The basic simulation software is also presented here.

Chapter Four describes the samples preparation of the III-nitride heterostructures with various growth conditions. The fabrication of AlGaN based device and characterization of the samples are also described in this chapter.

In **Chapter Five**, the results of structural, optical and electrical properties of $\text{Al}_x\text{Ga}_{1-x}\text{N}$ films are presented and discussed. **Chapter Six** discusses the results of metal contacts. **Chapter Seven** presents the results of the experimental and simulation results of the fabricated devices. Finally, the conclusions and future works are presented in **Chapter Eight**.

CHAPTER 2

LITERATURE REVIEW AND THEORETICAL BACKGROUND

2.0 Introduction

III-nitride semiconductors have a wurtzite crystal structure and a direct wide energy band gap. The band gap values range from 0.7 eV for InN, 3.4 eV for GaN, and 6.2 eV for AlN (Briot et al., 2004). Additionally, InN and AlN can be alloyed with GaN. These alloys allow the tuning of the band gap and emission wavelength. Due to these properties, III-nitrides have widely been used for violet, blue and green light emitting devices and for high power/high temperature transistors.

In this chapter, a number of growth techniques and parameters that influence the crystalline quality will be discussed. The basic theories of metal-semiconductor contacts are also addressed. Then, the basic principles of metal-semiconductor-metal (MSM) photodetector and high electron mobility transistor (HEMT) devices will be described.

2.1 Growth Techniques of III-Nitride Group

Epitaxial growth techniques have specifically been developed to enable the growth of high-quality semiconductor alloys under controlled conditions. Using these techniques, single-crystal semiconductor thin films can be synthesized on different substrates. Some researchers have successfully utilized metal organic chemical vapor deposition (MOCVD), hydride vapor phase epitaxy (HVPE) and molecular beam epitaxy (MBE) techniques, because so far they have greatly improved film quality. Therefore, these three techniques will be discussed briefly in the following sub-sections.

2.1.1 Metal-Organic Chemical Vapor Deposition (MOCVD)

The first systematic effort to grow III-nitride materials by chemical vapor deposition or sputtering processes took place in the 1970s in order to characterize the optical and structural properties of thin films. For example, in 1971, Manasevit et al. (1974) utilized metal-organic chemical vapor deposition (MOCVD) to grow GaN and AlN thin films on sapphire and silicon carbide (SiC) substrates. Then, Ejder (1974) used MOCVD technique to grow GaN films. After that, intensive studies to grow III-nitride materials using this technique were done by several researchers (Keyvan et al., 1986; Schwetlick et al., 1989; Schoen et al., 1998; Fareed et al., 2000; Jin et al., 2004). Up to now, MOCVD still remains the most popular growth method for III-nitride groups.

MOCVD is a technique used for depositing thin layers of atoms onto a semiconductor wafer. By using MOCVD, one can construct many layers where the thickness of each layer can be accurately controlled to create material with specific optical and electrical properties. This technique also allows to build a range of semiconductor photodetectors and lasers; the devices that lie at the heart of the information revolution. MOCVD approach was chosen over MBE growth technique because of its flexibility in growing precise controlled layers for special applications; it is typically done under near atmosphere pressure and it can be scaled up to industrial-scale production with relative ease. However, the disadvantages of MOCVD are: the reactants are very expensive compared with MBE and these reactants tend to be volatile, flammable and toxic (Morkoc, 1999). Moreover, the control of MOCVD processes is far more complex than MBE because there are many variables involved in the process.

MOCVD processes involve a series of complex reactions between different precursors. Appropriate precursors in MOCVD growth should exhibit sufficient volatility and stability to be transported to the surface. Furthermore, the precursors should also have suitable reactivity to be decomposed thermally into the preferred solid and to generate readily removable gaseous side products. Therefore, the precursors must be non-toxic, non-corrosive, non-pyrophoric, water- and oxygen-insensitive. Figure 2.1 shows the schematic illustration of a typical MOCVD.

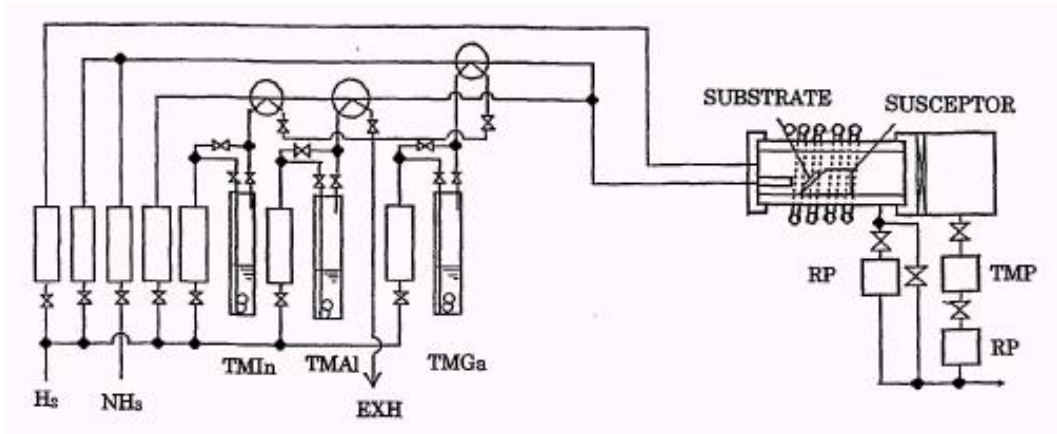


Figure 2.1: The schematic diagram of a typical MOCVD growth reactor [adopted from Morkoc (1999)].

In the atmospheric pressure MOCVD reactor, trimethylgallium (TMGa), triethylgallium (TEGa), trimethylaluminum (TMAI), and trimethylindium (TMIIn), turn out to be adequate column III precursors (Sheng et al., 1988; Morkoc, 1999). For the column V precursor, mainly research groups usually use NH_3 on a substrate heated to around $1000\text{ }^\circ\text{C}$; however, only some groups of researchers have tried to use microwave-activated nitrogen (N_2) in their experimental growth of nitride films. Besides these precursors, a carrier gas has to be used during MOCVD epitaxial growth. Hydrogen (H_2) is usually used as a carrier gas whenever indium is not incorporated in the epitaxial film. Nevertheless, when indium is incorporated in the

growth process, nitrogen is used rather than hydrogen because it fosters the incorporation of indium which tends to be desorbed easily from the substrate. According to Ludowise (1985), the reaction that explains III-nitride materials in MOCVD reactor, can be described by the following equation:



where R is an alkyl group such as methyl (CH₃) or ethyl (C₂H₅) and M is the III-nitride group materials such as gallium (Ga), indium (In) and aluminum (Al). The general III-nitride group sources used for MOCVD exist in either a liquid or a solid form. A carrier gas such as H₂ or N₂ is used to carry the metalorganic precursors to the reaction chamber.

2.1.2 Hydride Vapor Phase Epitaxy (HVPE)

HVPE technology was introduced more than 30 years ago to deposit single crystal layers of both GaN and AlN (Maruska and Tietjen, 1969; Yim et al., 1973). Because GaN materials are well-recognized as potentials for light emitters, several attempts to create GaN-based blue light emitting diodes by HVPE, including the revelation of the first GaN violet light emitter have been taken in the early 70's (Pankove et al., 1971). Early attempts to grow AlGaN alloys by HVPE method were reported by Hagen et al. (1978) where Ga and Al were transported to the reaction zone as subchlorides by passing HCl diluted with nitrogen gas over mixed melt Ga and Al in the graphite boat. After that, HVPE used for GaN materials shifted to substrate applications (Naniwae et al., 1990). High deposition rate intrinsic to GaN HVPE method and capability to form thick single crystal GaN layers on

unfamiliar substrates have led to intense developments in the field and to the showing of the first large area (3 cm diameter) GaN free standing wafers (Melnik et al., 1998). The later developments of HVPE technology for free standing GaN wafers by Look et al. (2003) resulted in the electron mobility of $1320 \text{ cm}^2/\text{V}\cdot\text{sec}$ and donor concentration of $7.8 \times 10^{15} \text{ cm}^{-3}$ in GaN materials.

Figure 2.2 shows the schematic typical HVPE of GaN growth. For GaN growth, source materials are gallium chloride and ammonia gases. Gallium chloride is formed inside the growth apparatus by the reaction of gaseous HCl and Ga metal.

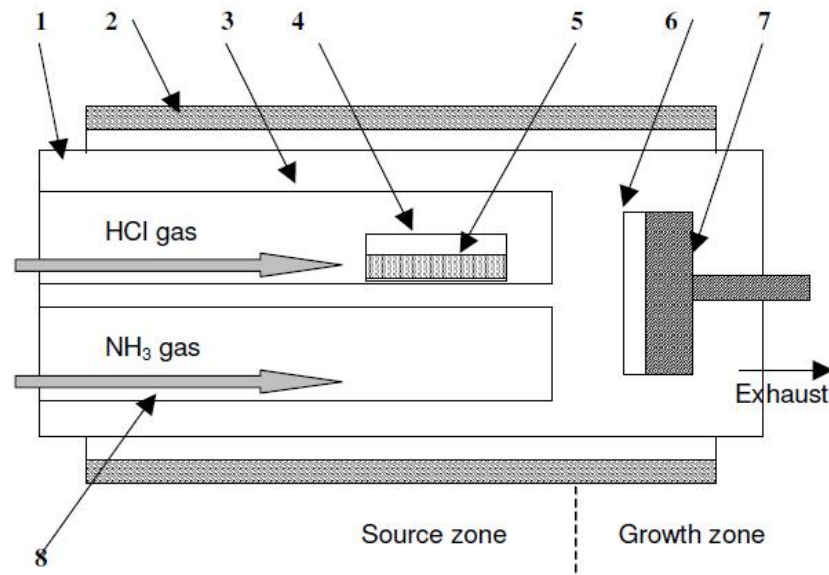


Figure 2.2: Schematic illustration for GaN HVPE growth: 1. main reactor tube, 2. heating elements, 3. Ga source gas channel, 4. boat with Ga melt, 5. Ga melt, 6. substrate, 7. substrate holder, and 8. ammonia source tube [adopted from Molnar (1998)].

The formed gallium chloride is transported to the growth zone of the system where it reacts with the ammonia forming GaN. When the substrates are located in the growth zone and substrate parameters are suitable, single crystal GaN is formed on the substrate. This method provides deposition rates of several microns per minute making it possible to grow hundred microns thick layers.

Nevertheless, in spite of substantial progress in material quality and process understanding, background n-type carrier concentration in the materials remained high and p-type GaN materials have not been fabricated then. In addition, HVPE is preferred to fabricate template substrates due to high growth rate, low defect density in the grown materials, and relatively low cost.

2.1.3 Molecular Beam Epitaxy (MBE)

MBE is a growth technique which has been developed by Cho in 1971. Cho stated that growth by MBE could be done atomically in the form of flat ordered layers; thus these studies marked the beginning of the use of MBE for practical device fabrication. Cho and Casey demonstrated how to incorporate doping impurities, and ultimately, how to fabricate GaAs–Al_xGa_{1-x}As laser structures, which at that time was considered a key test for III–V materials process (Cho and Casey, 1974). After that, MBE moved from being a novel but very uncertain film growth method to become an established research tool in which general directions for future work were well established. Since then, MBE research has rapidly increased, by publishing several books, monographs and conference proceedings (Cho and Arthur, 1975; Cho, 1983; Tu and Harris, 1990; Tsao, 1993; Sitter & Sitter, 1996).

MBE is considered the forefront of basic research because it can investigate the interfaces, including special materials such as polar and non-polar materials and strained heteroepitaxial structures. There is a need to use the MBE to fabricate some devices such as high-mobility modulation doped heterostructures as it is the only possible method to fabricate such devices. This means that MBE systems are now effective enough to compete with the traditional growth methods. One of the most important advantages of MBE is that dangerous chemicals can be handled in a solid

form and contained within the vacuum vessel, thus reducing the cost of external safety measures.

The major advantages of MBE over other techniques, which make MBE the best tool for basic research as well as for producing devices, can be summarized herein (Molnar et al., 1995). MBE allows a very accurate control of layer thickness and dopant incorporation down to the atomic scale. MBE usually performs at relatively low temperatures of 650 to 800 °C. Various sources can be turned on and off rapidly using the shutter, allowing MBE to comfortably make abrupt composition changes within a monolayer. The ultra-high vacuum (UHV) environment in the growth chamber allows the application of different *in situ* measurement techniques to study the processes governing crystal growth. As a result, these measurements can be used to implement real time feedback loops for growth control. Toxic chemicals are contained within the vacuum chamber. Compared to other growth techniques, no complicated chemical reactions take place on the substrate surface. This facilitates the analysis of growth processes such as surface migration and dopant incorporation.

However, in comparison with other techniques, there is one main disadvantage; MBE has slow growth rates, typically one to three monolayers per second, approximately 0.3 to 1 μm/hr (Johnson et al., 1996). For this reason, a number of MBE techniques, such as plasma-enhanced MBE and reactive-ion MBE, have been developed for AlGaIn/GaN heterostructure growth. MBE is practical as it functions in a flexible and simple way. For example, in an ultra-high vacuum (UHV) environment, beams of atoms or molecules are directed onto a heated substrate crystal to form a crystalline layer. Figure 2.3 shows the diagram of MBE growth chamber system.

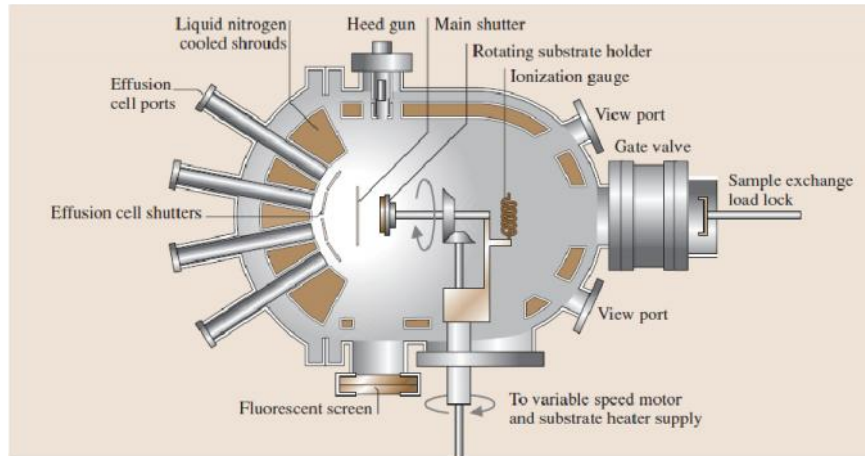


Figure 2.3: Schematic diagram of MBE system for the deposition of III-V semiconductor compounds [adopted from Cho (1983)].

First the substrates are loaded inside the growth chamber using vacuum load lock system. During the growth process, the elemental sources are heated inside Knudsen cells and evaporated at a suitable rate depending on the substrate temperature under UHV conditions. For III-nitride group growth, the effusion of the metal atoms (Ga, In, Al) and dopants (Si, Mg) through conventional Knudsen effusion cells has to be combined with a source for nitrogen radicals. MBE under UHV condition is compatible with a wide range of surface analysis techniques, such as reflection high energy electron diffraction (RHEED) and quadrupole mass spectroscopy for gas analysis. As mentioned before, MBE growth is usually performed at relatively low temperatures around 650-800 °C compared with other techniques. However, the molecular nitrogen is static and does not chemisorb on a GaN surface below 950 °C owing to strong N-N bond of the nitrogen molecule. Therefore, nitrogen that contains molecules with weaker bonds, should be provided. However, III-nitride group can be grown by plasma-assisted molecular beam epitaxy

where the plasma-induced fragmentation of nitrogen molecules is combined with the evaporated metal atoms from the effusion cells.

Therefore, the radio frequency (RF) or electron cyclotron resonance (ECR) plasma sources are commonly employed to activate the nitrogen species. The RF plasma source (13.56 MHz) (see Figure 2.4) was used to generate active nitrogen flux. The plasma sources are operated at nitrogen flow rate which produces a downstream pressure in the MBE chamber of 5×10^{-6} to 4×10^{-4} Torr. The RF plasma can be operated at powers between 150 and 600 W and pressures of 10–100 Torr.

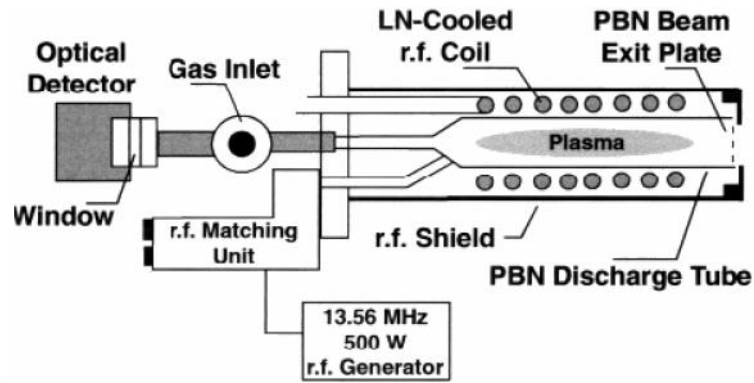


Figure 2.4: RF plasma source for producing nitrogen atoms [adopted from Hoke et al., (1991)].

2.2 Growth of AlGa_N Ternary Alloys

AlGa_N has received much attention among III-V nitride alloys for its potential applications in AlGa_N/Ga_N heterostructure devices. Hence, to grow this structure, there is a need to study the parameters that affect growth process to obtain good quality with different mole fractions. AlGa_N alloy has been grown by using different techniques such as HVPE, MOCVD and MBE (Ahn et al., 2005; Fareed et al., 2000; Zhang et al., 2005).

2.2.1 Influential Parameters in AlGaN Film Quality

There are several parameters that affect the AlGaN film quality. These parameters can be explained in the following sub-sections.

2.2.1.1 Substrates Parameter

The selection of a suitable substrate is very essential to grow structure with good quality. Therefore, the obstacles of growing AlGaN/GaN with different mole fraction are the lack of a suitable lattice match and thermally compatible substrate material. Table 2.1 shows lattice constant and important properties of III-nitride materials and substrates.

Table 2.1: Lattice constants, thermal expansion and lattice mismatch of substrates (Jain et al., 2000; Hanser et al., 1999; Vaillant et al., 1997)

Substrates	Lattice constant (nm) (a;c)	Thermal Expansion (10^{-6} K^{-1})	Lattice mismatch to hexagonal GaN %
Si (111)	(0.5430; -)	3.59	17
Sapphire	(0.4759; 1.2990)	7.30	16
6H-SiC	(0.3081; 1.5120)	4.46	-3.1
GaN	(0.3189; 0.5185)	5.59	-
AlN	(0.3112; 0.4982)	4.2	-2.4

Silicon is a very attractive substrate for AlGaN/GaN epitaxy because it offers large area wafers at a low cost with good thermal conductivity. Both zincblende and wurtzite AlGaN/GaN epilayers have been grown on Si (001) through MBE, MOCVD, and HVPE (Rossner et al., 1995; Kung et al., 1995; Kim et al., 1999). However, silicon has a large lattice mismatch (about 17%) and a high thermal expansion coefficient mismatch, which results in cracks on the surface and a high dislocation density (Jothilingam et al., 2001). Owing to the large lattice constant mismatch, it is difficult to grow pure zincblende phase GaN directly on the Si(001). Moreover, when exposed to reactive nitrogen sources, the silicon surface forms an

amorphous silicon nitride (SiN) layer which deteriorates the epitaxial layers. To prevent SiN formation, a few monolayers of aluminum were deposited on the surface before the nitride growth is commenced (Schenk et al., 1999; Wu et al., 2003; Calleja et al., 1999).

There were few attempts to correlate the surface phase diagram of Al on Si (111) and the Al monolayer thickness with the GaN epitaxial layer quality (Groger and Barczewski, 2001). Si (111) is generally the favorite substrate for AlGaN/GaN epitaxy due to the hexagonal-like arrangement of Si atoms on the (111) plane ((Liu et al., 2007). However, the quality of AlGaN based on this Si substrate has significantly been improved, and thus enhancing the performance of the fabricated devices such as high electron mobility transistors (HEMTs), metal semiconductor field effect transistors (MESFETs) and metal-semiconductor-metal photodetectors (Saito et al., 2005; Asgari et al., 2006; Pau et al., 2001).

On the other hand, sapphire (Al_2O_3) substrate has been used as a substrate for AlGaN/GaN epitaxial layer. The main reasons for using this substrate can be summed up here. Much more research has gone into developing procedures for producing good quality films on it compared to other substrates. Sapphire is stable at high temperature which is suitable to grow AlGaN/GaN thin films by MOCVD method (Morkoc 1999). The large lattice constant between GaN and sapphire makes the film completely relaxed (not strained) from the beginning of growth process. In addition, the sapphire substrate has a low thermal conductivity and thus resulting in a low dissipation heat sink. Generally, the c-plane sapphire substrate is usually used for AlGaN/GaN layer with a suitable buffer layer. AlGaN/GaN on the sapphire substrate has been grown by several techniques such as HVPE, MOCVD and MBE (Ahn et al., 2005; Chen et al., 2005; Zhang et al., 2005).

Silicon carbide (6H-polytype) has a number of advantages over sapphire for GaN epitaxy, such as a smaller lattice constant mismatch (3.1%) for (0001) oriented films and a much higher thermal conductivity (3.8 W/cm K) (Hanser et al., 1999). Conductive substrates are available, making electrical contacts to the backside of the substrate possible, thereby simplifying the device structure compared to sapphire substrates. Therefore, this substrate is suitable for high power and high temperature applications (Bremser et al., 1996; Gaska et al., 1998; Johnson et al., 2002). However, this substrate has few disadvantages; it is costly and has a small area.

2.2.1.2 Buffer Layers

As mentioned before, the large lattice constant mismatch between the substrate and AlGaN/GaN layers causes some cracks on the epilayer. Therefore, using buffer layer is essential to enhance the lattice constant match and improve the structure quality. The insertion of the buffer layer between the film and the substrate can release the strain of epilayer which reduces the cracks during the growth process. Furthermore, the direct growth of AlGaN/GaN film on the Si(111) surface develops a thin amorphous layer between the film and the substrate surface, most probably Si_xN_y , generated by the reaction of the Si surface with active nitrogen. The formation of such amorphous layers was reported by Ohani et al (1994). Therefore, the growth on Si substrates is very difficult and challenging. To avoid this amorphous layer formation, one needs to start the growth with an AlN buffer layer because the bond formation between Al and N atoms prevails over the Si-N one. Simultaneously, the AlN buffer layer strongly favors the subsequent growth of the GaN because the ratio of the match between atomic planes of Si and AlN is 4:5 (Stevens et al., 1995). Another method to prevent this amorphous layer formation is to deposit a few Al

monolayers on the clean Si surface before turning on the plasma source. Then, an AlN buffer layer is grown (Chin et al., 2008). In addition, the AlN high crystalline quality is required in order to achieve a two-dimensional (2D) growth mode (Calleja et al., 1997). Many researchers use an AlN buffer layer to obtain a GaN film of high quality due to the high thermal stability of AlN (Liu et al., 2007; Tsukihara et al., 2007). Watanabe et al., (1993) reported that a thin single crystal of AlN is an effective buffer layer to grow a single crystalline GaN on a Si substrate.

To grow AlGaN/GaN epitaxial films on sapphire, AlN is commonly used as the buffer layer (Liu and Andersson, 2004; Lisesivdin et al., 2007). When growing $\text{Al}_x\text{Ga}_{1-x}\text{N}$ with mole fraction x above 10%, the film with device quality could not be obtained and the film will have a high dislocation density (Tsukihara et al., 2007). Therefore, the insertion of AlN buffer layer is essential to reduce this dislocation and improve the crystalline quality.

2.2.2 Doping $\text{Al}_x\text{Ga}_{1-x}\text{N}$ Alloys

The growth of high quality doped $\text{Al}_x\text{Ga}_{1-x}\text{N}$ films is essential for the advanced electronic and optoelectronic devices. In spite of the considerable efforts in fabricating AlGaN-based devices, there have been intensive studies on the growth and characterization of $\text{Al}_x\text{Ga}_{1-x}\text{N}$ alloys; this is especially true when x is greater than 0.3. It has been observed that the conductivity of doped $\text{Al}_x\text{Ga}_{1-x}\text{N}$ decreases with increasing x . The high density defects can also be realized as dopants when the Al mole fraction increases (Iwaya et al., 2000). In addition, the increased doping reduces the carrier mobility because of impurity scattering. The types of doping are discussed in following sub-sections.

2.2.2.1 n-type AlGa_xN Doping

Al_xGa_{1-x}N systems are very suitable for the UV devices applications as they cover wavelengths ranging from 200 to 364 nm (Monroy et al., 2003). However, it is rather difficult to develop high conductivity n-type AlGa_xN alloys with high Al mole fraction ($x > 0.2$) which are indispensable to achieve high performance in UV devices (Khan et al., 2005). Both Si and Ge doping are used to obtain a high doping concentration of n-type of III-nitride group; while, Si-doping is usually used due to its higher solubility in III-nitride groups. A number of researchers have used different methods for Si-doping of n-type AlGa_xN and made great progress (Tahtamouni et al., 2008; Cantu et al., 2003; Kim and Jin, 2003). The Si atoms are incorporated onto Ga site and thus becoming electron donors. These donors are easily ionized because of their small activation energy, approximately 17 meV (Gotz et al., 1996). However, when Al mole fraction x increases, doping becomes more difficult.

Furthermore, it was found that the electrical activity of the n-type dopant Si decreases when x increases in the Al_xGa_{1-x}N crystal. Polyakov et al., (1998) explained the reduced electrical activity through an observed increase of the Si ionization energy with composition. Boguslawski and Bernholc, (1997) proposed that Si acts as a shallow donor when x is smaller than 0.5, but it forms a deep level defect (DX) center at $x \approx 0.60$. In contrast, Stampfl et al. (1999) argued that the reduced conductivity results from compensation by native defects with acceptor character.

Several researchers reported the electron concentration of Si-doped AlGa_xN grown by using MOCVD and MBE techniques. For example Cantu et al. (2003) reported n-type carrier concentration equal to $2.5 \times 10^{19} \text{ cm}^{-3}$. In addition, Ahoujja et al. (2002) found the carrier concentration in the range of $(4.5-19) \times 10^{18} \text{ cm}^{-3}$ for